ASME Journal of Offshore Mechanics and Arctic Engineering
Online journal at:
https://asmedigitalcollection.asme.org/offshoremechanics

Field Investigation of Bluff Body, Spring, Damping, and Mechanical Rectification Performance Impacts on a Galloping Current Energy Converter

Benjamin Loeffler[1]
Alaska Center for Energy and Power,
University of Alaska Fairbanks,
1764 Tanana Loop, Suite 404,
Fairbanks, AK 99775
e-mail: bhloeffler@alaska.edu

Paul Duvoy
Alaska Center for Energy and Power,
University of Alaska Fairbanks,
1764 Tanana Loop, Suite 404,
Fairbanks, AK 99775
e-mail: pxduvoy@alaska.edu

Jeremy Kasper
Alaska Center for Energy and Power,
University of Alaska Fairbanks,
1764 Tanana Loop, Suite 404,
Fairbanks, AK 99775
e-mail: jlkasper@alaska.edu

David Denkenberger
Department of Mechanical Engineering,
University of Canterbury,
Private Bag 4800,
Christchurch 8140, New Zealand
e-mail: david.denkenberger@canterbury.ac.nz

The Water Horse is a galloping current energy converter, originally developed by Renerge Inc., which uses flow-induced oscillation to harness riverine hydrokinetic energy and convert it to electricity through a novel power takeoff (PTO) system. This article presents the correlational analysis of data collected during field testing of a Water Horse prototype at the University of Alaska Fairbanks (UAF) Tanana River Test Site in the summer of 2020. Testing focused on investigating the impacts of various system parameters on system level performance. Specifically, variations in bluff body sizing, spring stiffness, generator damping, and mechanical rectification of shaft rotation were correlated with oscillation frequency, oscillation amplitude, electrical output power, and water-to-wire efficiency. Completed at Reynolds numbers of 700,000 to 1,100,000, these data provide insight into galloping energy harvesting at the kW scale in a typical Alaska riverine environment. The bluff body with a smaller diameter and length delivered higher electrical power output than the larger bluff body; however, energy transfer into the floating platform was qualitatively higher with the larger bluff body. Removal of mechanical rectification led to increases in power production and system efficiency while decreasing peak-to-average power levels at the generator. The data show that optimal damping was not reached due to force limitations in the PTO design. Overall, total conversion efficiency was low, reaching a maximum total efficiency of 1.8% for the design swept area and a maximum specific efficiency of 2.6% for the actual swept area. [DOI: 10.1115/1.4069998]

Keywords: fluid–structure interaction, ocean energy technology, vortex-induced vibration, hydrokinetics

1 Introduction

1.1 Riverine Hydrokinetic Energy and Alaska.

Alaska is home to over 90 geographically and electrically isolated communities that abut rivers and consume a collective 175,000 MWh per year, predominantly from diesel generators [1]. These riverine microgrids range in average load from 10 kW to 5 MW, far below what might justify investments in civil engineering infrastructure such as dams or diverters. Furthermore, dams and diverters are likely to significantly impact habitat for species core to subsistence lifestyles [2]. In contrast, there is a reason to believe that the environmental impacts of discrete hydrokinetic devices may be acceptable [3–6]. For this reason, hydrokinetic current energy converters (CECs) have long been of interest to remote riverine communities seeking to generate electricity from local river energy resources.

A 2014 assessment of riverine energy resources in 22 Alaska communities on the Yukon, Kuskokwim, and Copper rivers predicted riverine energy resources at average discharge ranging from 800 kW to 8.6 MW [7]. A further study has investigated interconnection distances and costs based on these data [8]. Despite these efforts to measure resources and quantify interconnection feasibility, economically viable CEC have not yet seen widespread adoption in Alaska riverine communities. Two major impediments to hydrokinetic power generation in Alaska have been (1) CEC device susceptibility to damage from woody debris in the river and (2) the high cost and complexity of hydrofoil turbines and submerged rotating and electrical components [9,10]. Attempts at deploying grid-connected CEC were undertaken in the Yukon River at the communities of Eagle and Ruby between 2008 and 2010. In both cases, woody debris common to the river caused

---

[1] Corresponding author.

Contributed by the Ocean, Offshore, and Arctic Engineering Division of ASME for publication in the JOURNAL OF OFFSHORE MECHANICS AND ARCTIC ENGINEERING. Manuscript received May 24, 2025; final manuscript received September 9, 2025; published online November 19, 2025. Assoc. Editor: Ryan Coe.

frequent stoppage of the turbines and both projects were ultimately discontinued [9]. A long-running project in the Kvichak River at Igiugig has achieved several milestones [11]; however, the Kvichak River does not expose the CEC to debris and sediment at the levels seen on the Yukon or Kuskokwim River.

1.2 Tanana River Test Site. The experiences at Ruby and Eagle were the motivation for the establishment of the Tanana River Test Site (TRTS) by the Alaska Center for Energy and Power (ACEP) at the University of Alaska Fairbanks (UAF). TRTS is situated on the Tanana River, a tributary of the Yukon, in the town of Nenana, AK, and is road accessible 55 miles from Fairbanks. TRTS provides a fully permitted and accessible testing ground in a representative Alaska riverine environment. With a typical depth of 8–9 m and a summer flow velocity ranging from 1.5 to 2.5 m/s, the test site is well suited for testing kW-scale CEC. A variety of published research has resulted from research and testing activities at TRTS [12–17]. A map of the permitted stretch of river and representative acoustic Doppler current profiler (ADCP) transects plots is shown in Fig. 1. The thalweg path is the line of maximum depth of the river channel. The maximum path is the line of maximum velocity.

1.3 Introduction to Flow-Induced Oscillation. Both vertical and horizontal axis cross-flow, as well as axial-flow, turbines have demonstrated susceptibility to negative consequences of debris impacts and accumulation. All technologies evaluated prior to this work are not compatible with naturally occurring debris and will likely require a debris mitigation system in uncontrolled rivers, adding to the cost and complexity of the installation. This work evaluates an alternative approach in which flow-induced oscillation (FIO) is harnessed to convert kinetic energy in the flowing river into mechanical oscillations, which are in turn converted into electricity through a purpose-built power takeoff (PTO).

The term “gallop” refers to aeroelastic instability of structures that result in self-excited oscillations under the incident fluid flow (commonly air or water). When an elastically constrained structure is immersed in a flowing fluid, “negative damping” can occur in which fluid forces on the structure induce motions that generate larger fluid–body forces. Early studies of gallop focused on understanding the phenomenon for the purposes of mitigation, as such oscillations can be damaging to the infrastructure [18–20]. It should be noted that these oscillations are produced by forces generated by fluid–body interactions resulting from the motion of the structure relative to the fluid. Gallop is distinct from resonance and can occur at frequencies significantly different than the resonant frequency of the mass–spring–damper. A rigorous assessment of the noteworthy Tacoma Narrows Bridge collapse makes this distinction clear and attributes the bridge failure to “self-excitation” in the torsional degree-of-freedom [21]. More recently, substantial efforts have been made to harness FIO, including both gallop and vortex-induced vibration, for the capture of hydrokinetic energy [22]. The Marine Renewable Energy Lab at University of Michigan has published extensively on flume testing data and advanced development of associated PTO and controls of the VIVACE Converter [23–31]. In particular, hydrodynamic efficiencies of up to 88.6% of the Betz limit have been demonstrated in multiple cylinder systems [32].

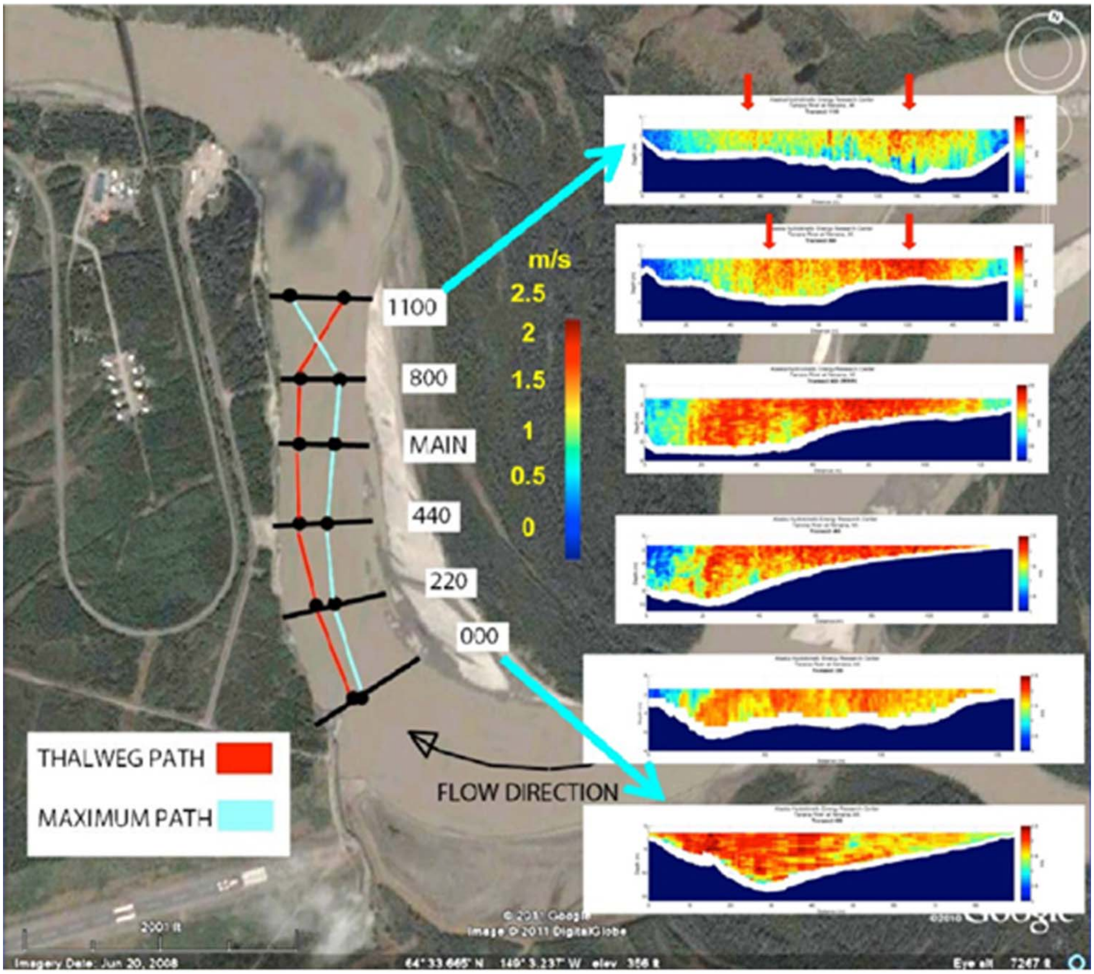

Fig. 1 Satellite view of Tanana River Test Site with ADCP transects. Deployment location is approximately at the MAIN transect in the region between the thalweg and maximum paths.

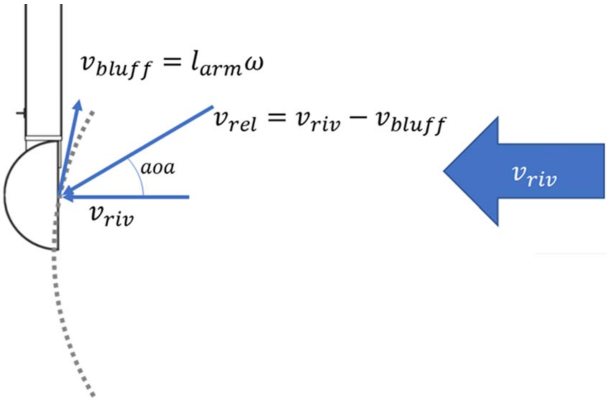

Fig. 2 Schematic of bluff body motion and relative velocity

The Water Horse is a vertically oscillating CEC technology initially developed by Renerge, Inc. [33,34] and further developed and field tested by ACEP. The Water Horse generates FIO by submerging a horizontal bluff body transverse to the water flow, suspended from a floating structure that houses the spring and PTO. As shown in Fig. 2, the bluff body is constrained by the suspension to move along a vertical arc. The relative velocity of the water incident on the bluff body, v_{rel}, is the vector sum of the velocity of the bluff body, v_{bluff}, and the river velocity, v_{riv}. When the bluff body is in motion due to the angular velocity of the suspension, ω, the relative velocity has an angle-of-attack, *aoa*, relative to the bluff body axis of symmetry and produces lift and drag forces on the bluff body that drive oscillations as constrained by the spring system and dissipated by the PTO.

The prototype Water Horse removes all sensitive electrical and mechanical components above the water line, reducing costs and risk of damage. Furthermore, by incorporating a simple break-away hinge in the bluff body support structure, the new design prevents structural damage from debris interaction and simplifies the recovery from such events. The hypothesis of this approach is that the Water Horse design permits a more robust and lower cost machine compared to hydrofoil turbines, while sacrificing hydrodynamic conversion efficiency (relative to lift-based turbines and the more sophisticated VIVACE) and producing a pulsed power output. If the capital cost (Capex) and operations and maintenance cost (O&M) reductions relative to conventional turbines outweigh any efficiency shortfalls, then lower levelized cost of energy (LCOE) is possible. This effort designed and built a kW-scale prototype and tested it at the Tanana River Test Site in the summer of 2020.

2 Methods

2.1 Overview of Prototype and Key Design Features. Key design criteria for the prototype development were to produce a rugged and readily field serviceable system utilizing commercial off-the-shelf (COTS) components and minimal custom-fabricated parts. Many components are cut-and-weld assemblies that could be readily mass produced. The prototype was designed to deploy from the aft end of the existing Tanana River Test Site research barge; however, for real-world applications, deployment could be from either the existing fixed infrastructure or a purpose-built or repurposed floating platform. An overview of the design of each subsystem is presented in Sec. 2.2.

2.2 Design Sizing Tool. While not the focus of this article, the prototype system design was informed by a numerical quasi-static model implementing lift and drag coefficients for the D-shaped bluff body from the literature [35] and Newtonian incremental equations of motion in polar coordinates with nonequilibrium initial conditions. This numerical model successfully predicted the limit cycle behavior of the oscillator under steady flow conditions and enabled consideration of the potential effects of various design parameters. No design optimization was performed; however, the model was used to aid in system and component sizing and selection. The prototype design prioritized the ease of manufacture, use of COTS components, and structural ruggedness for deployment in a harsh field environment. Schematics of the system design are presented in Figs. 3 and 4. The bluff body is interchangeable, and a smaller bluff body was used to reduce forces on the system during initial deployments. Key geometric design values for the prototype are reported in Table 1. Here, the oscillating mass is calculated from the measured weights and center of mass of the individual as-built bluff body, support, and suspension components. It does not include any "added mass" in the water or the mechanically coupled inertia of the spring and PTO systems. This sprung mass is used to predict the equilibrium position of the oscillator in the water.

2.2.1 Oscillator and Suspension. The D-shaped bluff body is supported by a vertical rectangular steel tube beam, which is in turn supported by upper and lower a-arms with greased sleeve bearings in the pivot ends to constrain motion to a vertical arc. The considerable cantilevered drag load on the bluff body results in the lower arms in tension and the upper arms in compression. At midstroke, the bluff body is approximately 1.34 m (54 in.) below the water surface. The arms are 1.53 m (60 in.) long and constrained by mechanical bump stops to a range of ±30 deg, for a total possible stroke of 1.53 m (60 in.). The a-arms connect to the structural frame, which houses the spring and generator subsystems. The structural frame is hinged to the barge deck at the forward end, with latches at the aft end to hold the frame in the down/deployed position. The system is shown in retrieved and deployed positions, respectively, in Figs. 5 and 6. The research barge hydraulic drum winches and lines are used to tilt the assembly into and out of the water for deployment and retrieval, while the barge is moored in the current study as described in Sec. 2.3.

The interchangeable bluff bodies were fabricated of rolled and welded aluminum sheet, with the large bluff body 2.43 m (96 in.) in length and 0.61 m (24 in.) in diameter and the small bluff body 1.82 m (72 in.) in length and 0.41 m (16 in.) in diameter. The total weight of the oscillating structure divided by the mass of displaced water at midstroke yields a specific gravity, or a mass ratio (MR) of 0.66 with the large bluff body and 1.64 with the small bluff body. Thus, the equilibrium deployed position for the large bluff body is above midstroke and that for the small bluff body is below midstroke. A mass ratio of 1.0 may help ensure symmetric utilization of the available stroke and thus should be considered for future design iterations. A photo of the two bluff bodies is shown in Fig. 7.

2.2.2 Spring System. The physical embodiment of the spring proved to be the most challenging aspect of the mechanical design of the prototype. The spring mechanism must be sufficiently stiff, act bidirectionally with smooth transitions, and allow large oscillator displacements. In this prototype, a tether (type 80H heavy duty roller chain) passing through opposing idler pulleys inside the oscillator arc was used to connect the spring lever arm to the oscillator support as shown in Fig. 4. The design is such that the springs are at minimum compression at mid oscillation and that oscillation up or down is resisted by compression of the springs via displacement of the tether.

The spring pack is assembled from commercially available coil springs, arranged in series and parallel with end plates and guide rods. A lever with an adjustable leverage ratio between the tether and spring pack is used to provide adjustment of the effective spring rate and travel at the tether connection. The spring lever contained five evenly spaced tether connection points, and the tether preload was adjusted via an inline turnbuckle, combining to allow for testing at different spring stiffnesses. The preload is necessary

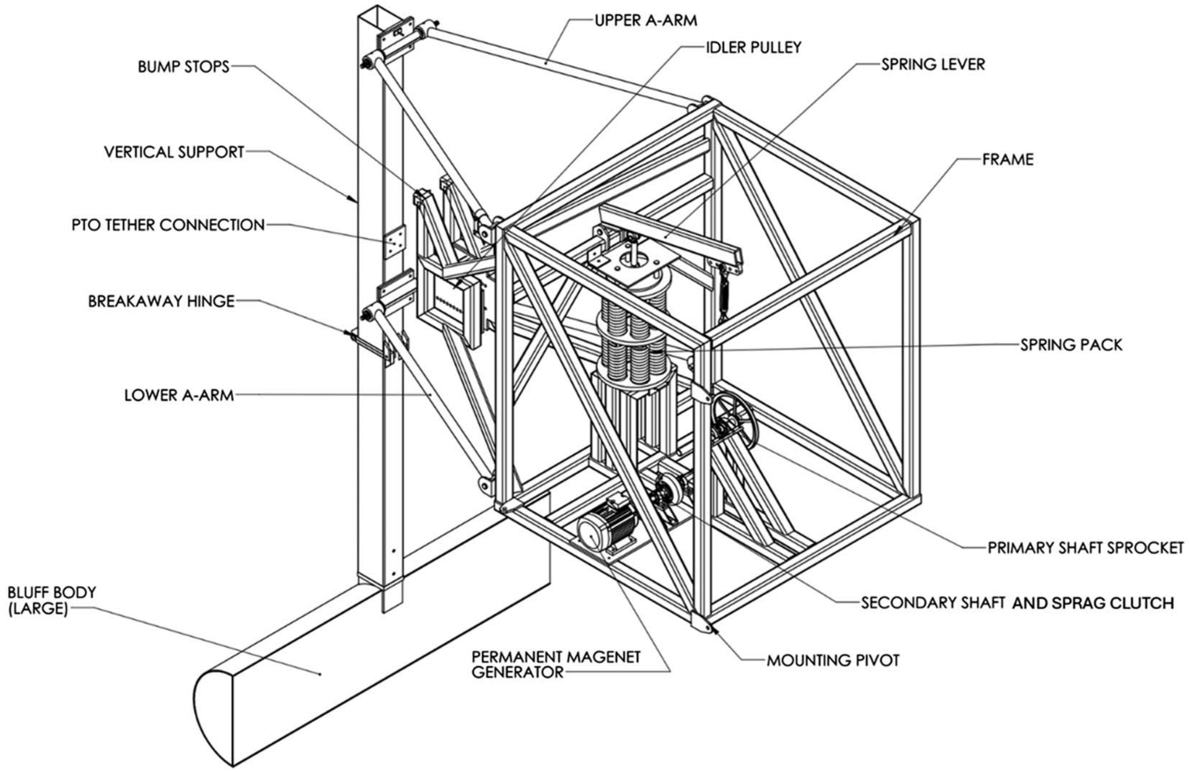

Fig. 3 Isometric view of Water Horse prototype design with key components and geometries notated

to ensure the springs are not unloaded at midstroke for a smooth transition of the bidirectional spring force. This arrangement produced a nonlinear spring force on the oscillator with lower effective spring rates near midstroke. To show the qualitative nonlinearity, an example plot of tether force as a function of oscillator angle is shown in Fig. 8. Through the geometric relationships of the prototype, this is converted to calculated torque on the oscillator, shown in Fig. 9.

2.2.3 Power Takeoff. The chain tether connecting the oscillator and spring lever was the connection point for the prototype PTO. The roller chain turned a toothed sprocket while traveling

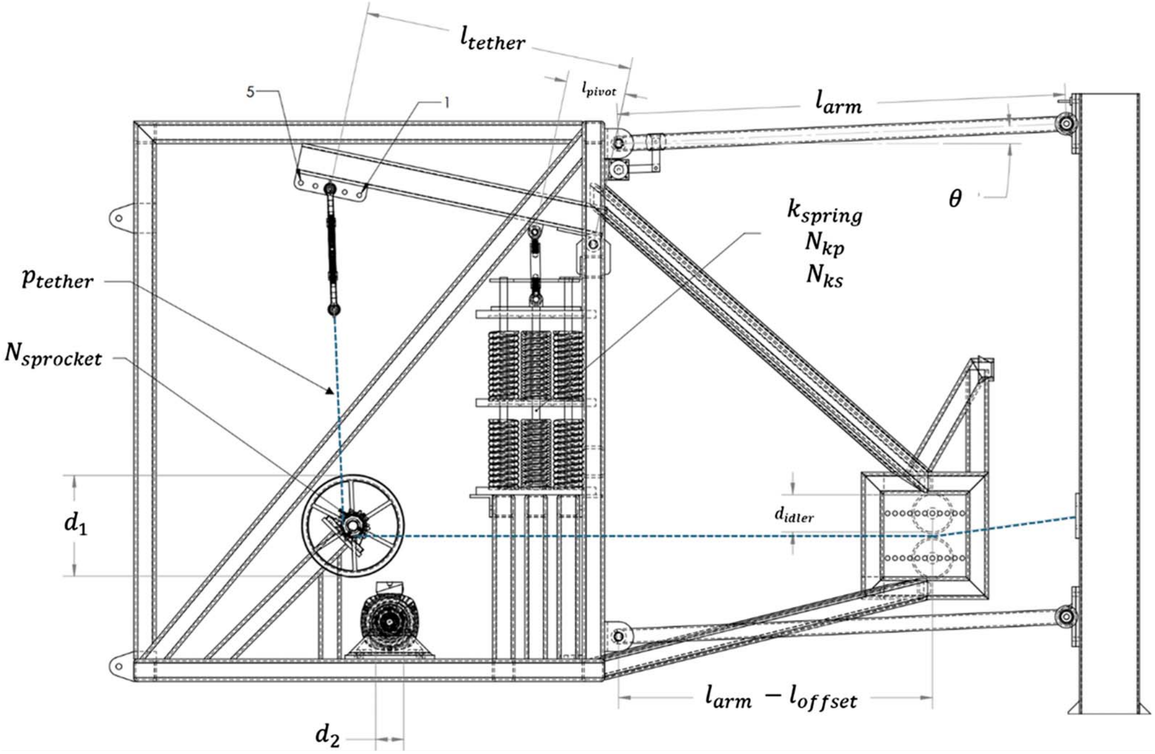

Fig. 4 Side view of Water Horse prototype with key geometries notated

Table 1 Water Horse prototype key geometric parameters.

Symbol	Description	Value	Units
D	Bluff body diameter	Large: 0.61 (24.0) Small: 0.41 (16.0)	m (in.)
L	Bluff body length	Large: 2.43 (96) Small: 1.83 (72)	m (in.)
m_{osc}	Oscillating mass	Large: 235 (517) Small: 195 (429)	kg (lb)
MR	Mass ratio (oscillating mass divided by displaced water mass at midstroke)	Large: 0.66 Small: 1.64	n/a
l_{arm}	Linkage length	1.53 (60.0)	m (in.)
$\theta_{\max}$	Max linkage angle	30	deg
k_{spring}	Individual spring constant	76 (675)	N/m (lb/in.)
N_{kp}	No. springs in parallel	7	n/a
N_{ks}	No. spring levels in series	2	n/a
l_{pivot}	Spring lever length	20.3 (8.0)	cm (in.)
l_{tether}	Tether lever length	Pos 1: 81.3 (32.0) Pos 3: 91.4 (36.0) Pos 5: 102 (40.0)	cm (in.)
d_{idler}	Tether idler diameter	12.7 (5.0)	cm (in.)
l_{offset}	Idler offset from oscillator	42.6 (16.75)	cm (in.)
p_{tether}	Tether chain pitch	2.54 (1.0)	cm/tooth (in./tooth)
N_{sprocket}	Sprocket tooth count	12	n/a
d_1	Primary pulley diameter	33.0 (13.0)	cm (in.)
d_2	Secondary pulley diameter	7.62 (3.0)	cm (in.)
r_{belt}	Belt speed ratio, $\frac{d_1}{d_2}$	4.3	n/a

between the spring lever and the idler pulleys, which engaged the permanent magnet generator (PMG) shaft via a belt and pulleys. The pulley system increased the rotation rate by a factor of 4.3. As the chain moves bidirectionally during each oscillation cycle, the reversing shaft motion was mechanically rectified by a one-way bearing or "sprag clutch" (FZ 6206 trade number) such that mechanical torque transferred to the generator only during the oscillations away from the neutral position, and the generator shaft freewheeled during the return motion. This sprag clutch was removed for a period of testing with the small bluff body and a comparison of performance with and without mechanical rectification is included in this analysis. The mechanical to electrical conversion occurred via a permanent magnet synchronous generator with built-in rectifier (Huber DSG P 112.14-10) rated at 7800 W at 500 VDC and 2000 rpm.

2.2.4 Power Dissipation. No active controls were implemented in this prototype testing. The direct current (DC) electrical power output from the generator was dissipated into a programmable DC load bank (NH Research 4760-6) operated in a constant resistance mode. By adjusting the resistance setting on the load bank, the PTO damping on the oscillator could be adjusted. While not included in this field testing, a power converter system was designed to accommodate the pulsed power output of the Water Horse PTO and provide regulated battery charging [36,37].

2.3 Field Test Conditions and Instrumentation. The deployment location at TRTS is located approximately at 64.561 deg N, 149.066 deg W. An overhead view of testing is shown in Fig. 10. The TRTS main buoy (right side of image) is chained to a

Fig. 5 Water Horse prototype in the "retrieved" position on TRTS research barge

Fig. 6 Water Horse prototype in operation off the aft end of the TRTS research barge

Fig. 7 Small (left) and Large (right) bluff bodies on deck of TRTS research barge between test deployments

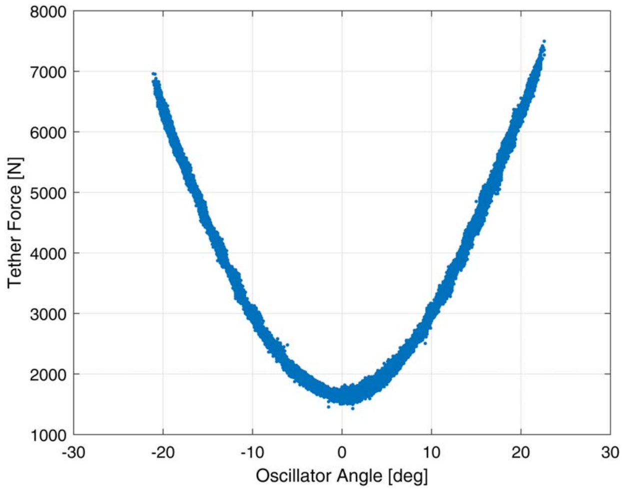

Fig. 8 Spring tether tension as a function of oscillator angle, showing a preload of approximately 1500N

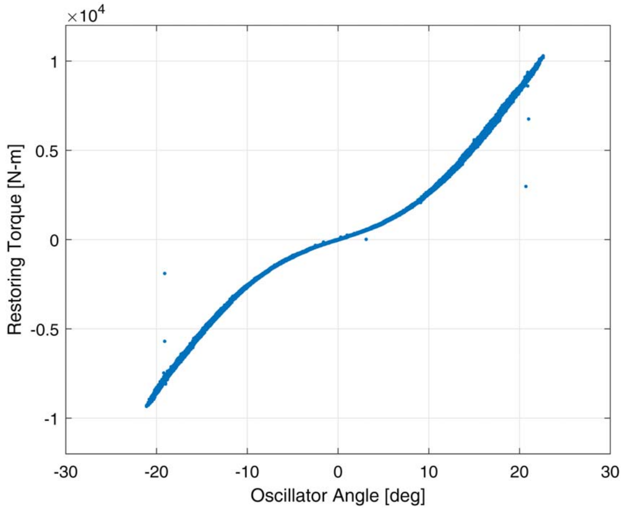

Fig. 9 Calculated torque of spring tether on the oscillator as a function of oscillator angle

permanent drag embedment anchor. A surface debris diverter [13,15] was positioned downstream of the buoy and upstream of the research barge to reduce the incidence of floating woody debris during testing. The research barge includes an instrumentation tent where the load bank and data acquisition hardware were housed and monitored. Downstream of the research barge was the inclined-plane fish trap [38], which was used to sample for fish during testing.

Prototype testing occurred between July 6 and 10, 2020. During this period, the United States Geological Survey (USGS) gauge at Nenana reported an average discharge climbing from 1700 m^3/s (60,000 cfs) to 2000 m^3/s (70,000 cfs) over the duration of testing, which is approximately 10% higher than the median daily discharge for those dates [39]. The water temperature averaged approximately 16 °C (61 °F), water density is assumed to be 999 kg/m^3, and dynamic viscosity is assumed to be 1.10×10^3 N-s/m^2.

The river depth at the deployment location was approximately 8 m, and the total river width is approximately 200 m. For this deployment, the blockage ratio of the river is well below 1% and assumed negligible.

Mechanical and electrical parameters were measured during field testing to enable investigation of performance and efficiency. A summary of the sensors is presented in Table 2. An inline load cell at the connection to the spring lever measured the tension in the spring tether. A rotary potentiometer and 3-bar linkage measured the angular position of the a-arm suspension and was used to calculate oscillator position and velocity. A strain gauge installed on a single suspension arm enabled validation of design calculations, but it is not used in this analysis. Three-axis accelerometers were installed on the Water Horse frame and the oscillator support to enable comparison of frame and oscillator accelerations. The DC electrical output voltage and current from the generator rectifier were measured to quantify electrical output power. The three-axis accelerometers were sampled at 100 Hz by a Campbell Scientific CR6 data logger. All other instruments were sampled at 50 Hz using a Campbell Scientific CR1000 data logger. All loggers were time-synced to GPS.

This work incorporated IEC TC114 62600-300 methodologies where possible, but does not implement the standard completely. Three-dimensional water velocity was measured using both ADCP and acoustic Doppler velocimeter (ADV). An RDI 600 kHz Workhorse ADCP was positioned approximately 12.7 m (500 in.) upstream of the bluff body in a downward orientation. This positioning of approximately 5.2 equivalent diameters, D_E, for the large bluff body slightly exceeds IEC 62600-300 recommendations but was necessitated by the layout of the research barge. Three-dimensional velocity measurements were rotated and resolved into streamwise, vertical, and horizontal components following established methods [40]. When ADCP data are available, the power-weighted average of the streamwise velocity in the depth bin centered at 1.45 m depth is used for calculations in this article.

With velocities in the range of 2.0 m/s, the water velocity incident on the ADCP is expected to reach the oscillator with a delay between 5 and 7 s. The analysis in this article utilizes data averaged over several minutes and does not account for this delay. With a depth of 8 m, the deployment location had a local Froude number of approximately 0.23. In this flow, the large bluff body has a Reynolds number on the order of 1,100,000 and the small bluff body has a Reynolds number on the order of 700,000.

Where acoustic doppler current profiler (ADCP) data are unavailable, acoustic doppler velocimeter (ADV) measurements at a depth of approximately 0.85 m are used for water velocity calculations. Where neither ACDP nor ADV measurements are available, a correlation [41] of measured velocity to USGS stream gage discharge is used to fill in gaps on a 15 min basis.

2.4 Testing Matrix.

Field testing presents the inherent challenge that many variables cannot be controlled. A primary

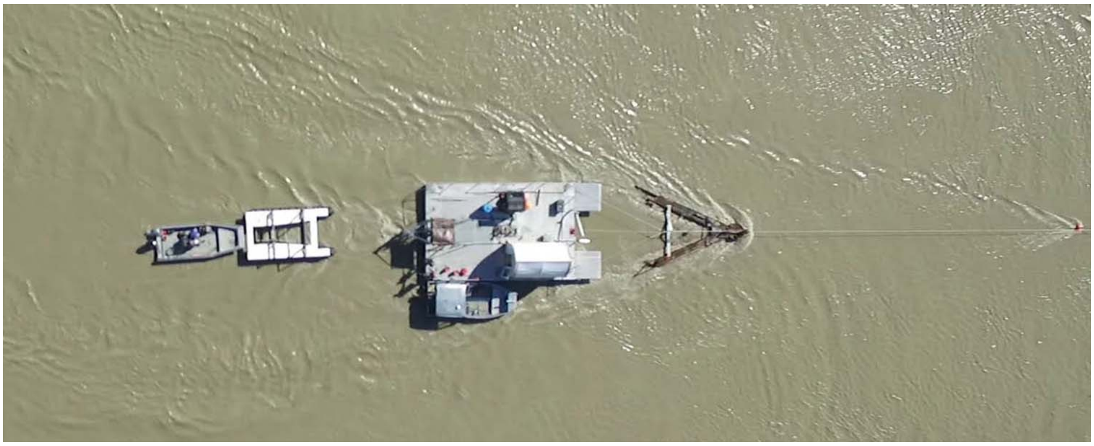

Fig. 10 Overhead view of TRTS testing infrastructure. Water flow is from right to left. Visible from right to left are buoy, mooring line, V-shaped debris diverter, research barge, and inclined-plane fish trap for fish monitoring.

example of an uncontrolled variable in open water testing is that the water velocity and turbulence are both in constant fluctuation, yet over the course of a given testing week may cover only a narrow range of possible values in the hydrokinetic system operating envelope. IEC 62600-300 addresses this reality by using temporal averaging and methods of bins. The analysis presented here largely uses averaging over approximately 10 min periods of operation at each system configuration to present data over a relatively narrow range of velocities encountered during testing. On a few occasions, testing was interrupted by mechanical issues or debris impacts and the data have been windowed to exclude these events. The independent variables explored in this study are (1) bluff body size, (2) spring stiffness (lever position), (3) generator damping (load bank setting), and (4) presence of mechanical rectification in the PTO. The total minutes of operation conducted at combinations of spring setting and load bank setting for the two bluff body sizes are presented in Tables 3 and 4.

The PTO and spring systems introduce inherent nonlinearities in the spring and damping constants as the oscillator moves through its range of motion. For this reason, correlational analysis in this report is conducted using spring connection points and load bank resistance settings, rather than measured spring and damping constant (k and c) values. The results section of this article examines data binned by combination of spring and load setting to explore correlations with dependent variables of oscillation amplitude, oscillation frequency, power output, and efficiency. In total, data were collected for over 12 h of operation at a range of configurations.

3 Results and Analysis

For each combination of bluff body, spring setting, and damping setting, the mechanical and electrical data were averaged across the duration of the test, and the power-weighted average of the streamwise velocity was calculated. A key aspect of field testing of hydrokinetic devices is exposure to uncontrolled turbulent conditions. Turbulence is not explicitly considered in this analysis; however, for the duration of the field testing data utilized in this article, the average streamwise turbulence intensity, defined as the ratio of the streamwise root-mean-square velocity to the streamwise mean velocity, at the mean bluff body depth was calculated to be 11% and ranged from 10% to 12% for any particular testing window.

A unique challenge of analyzing FIO performance is that the swept area of the device is variable over time and is not provided for in IEC 62600-300. For this reason, the analysis considers both the maximum design swept area, $A_{\text{swept,design}}$, which would be realized at $\theta_{\max}$, and the per-oscillation actual swept area, A_{swept}.

Table 2 Summary of instrumentation and data acquisition systems

Data logger	Channel name	Description	Sensor make and model	Sampling rate	Measurement range	Rated accuracy
Campbell Scientific CR1000	Volt	Generator terminal voltage	Magnelab DVT-1000-V05	50 Hz	10–1000 VDC	0.5% FS
	Amp	Load bank current	Magnelab DCT100-10-B-24-S	50 Hz	0–100 ADC	1% FS
	Angle	A-arm angle	AMCI DC25F-B1V1MS	50 Hz	0–90 deg	12 bit resolution (< 0.01 deg)
	Load	Chain inline load cell	LCC-HRS-10K	50 Hz	0–44 kN (0-10,000 lb)	0.01% FS
	Strain	Lower A-arm strain gage	BDI ST350	50 Hz	±4000 με	1% FS
Campbell Scientific CR6	Accel 1	Bluff body three-axis acceleration	BDI TA2512-0101	100 Hz	±10 g	18 $\mu g/\sqrt{\text{Hz}}$
	Accel 2	Support and Frame three-axis acceleration	BDI TA2512-0101	100 Hz	±10 g	18 $\mu g/\sqrt{\text{Hz}}$
WINRIVER PC software	ADCP	Deployed down-looking from bow of barge, 13 depth bins (0.5 m)	RDI 600kHz Workhorse	2.2 Hz	±5 m/s (default) up to ±20 m/s	±0.3% of measured velocity ± 0.3 cm/s
NORTEK VECTOR PC software	ADV	Deployed on lead fish from bow of barge, approximate depth of 0.85 m	Nortek Vector	16 Hz	±4 m/s	±0.5% of measured value ±1 mm/s

FS, full scale.

Table 3 Testing matrix of load bank setting and spring setting for small bluff body testing

Small bluff body—testing duration (min)				
	Spring lever position			
Load bank resistance setting (ohm)	1	3	5	Grand total
20	10	11	11	32
30	10	25	10	45
40	12	52	10	74
50	8	38	10	57
60	10	42	10	62
70	–	10	–	10
6000	10	27	11	48
Open circuit	–	10	–	10
Grand total	61	216	61	338

Note: Total minutes of instrumented operation in each combination are reported.

Table 4 Testing matrix of load bank setting and spring setting for large bluff body testing

Large bluff body—testing duration (min)				
	Spring lever position			
Load bank resistance setting (ohm)	1	3	5	Grand total
5	–	–	6	6
12	–	10	–	10
14	–	2	–	2
16	–	55	–	55
18	–	3	–	3
20	10	100	10	120
22	–	5	–	5
24	–	5	–	5
25	–	58	–	58
26	–	5	–	5
28	–	5	–	5
30	11	13	11	35
40	10	–	10	20
50	11	–	12	23
60	16	13	10	39
6000	11	11	10	32
Grand total	69	285	69	423

Note: Total minutes of instrumented operation in each combination are reported.

Within each dataset, a peak-finding function was used to identify local peaks in the oscillator angle, θ, and measurement time-series, and mark the beginning and end of sequential oscillation cycles, t_n. The oscillation frequency, f_n, of each cycle was determined by taking the inverse of the time elapsed between peaks, per Eq. (1).

$$f_n = \frac{1}{t_n - t_{n-1}} \tag{1}$$

For each cycle identified, the maximum and minimum oscillator angles, θ, measurement for the oscillation cycle, were used to calculate the maximum and minimum vertical oscillator positions, Z_{osc}, respectively, per Eq. (2). The stroke, S, of the individual oscillation cycle is the difference between the maximum and minimum oscillator position during that cycle, per Eq. (3). The swept area for each cycle is calculated using this stroke, as shown in Eq. (4).

$$Z_{\text{osc}} = Z_0 + l_{\text{arm}} \sin\theta \tag{2}$$

$$S = Z_{\text{osc, max}} - Z_{\text{osc, min}} \tag{3}$$

$$A_{\text{swept}} = (S + D_{\text{bluff}}) \times L_{\text{bluff}} \tag{4}$$

The design swept area is calculated as follows in Eqs. (5) and (6) using the design stroke, S_{design}.

$$S_{\text{design}} = 2l_{\text{arm}} \sin 30 \text{ deg} = l_{\text{arm}} \tag{5}$$

$$A_{\text{swept,design}} = (l_{\text{arm}} + D_{\text{bluff}}) \times L_{\text{bluff}} \tag{6}$$

The output power of the system is simply the product of the DC voltage and DC current measured at the interface between the generator output and the load bank input, Eq. (7). Thus, losses in the electrical rectification are lumped into the generator conversion efficiency.

$$P_{\text{elec}} = V_{\text{DC}} \times I_{\text{DC}} \tag{7}$$

The water-to-wire efficiency of the system is calculated on two bases. In both cases, the electrical output power is divided by the hydrokinetic power in the swept area of flow. The hydrokinetic power in the swept area, P_{swept}, is calculated per Eq. (8). However, due to the variable and asymmetric bluff body motions under different conditions, the swept area, A_{swept}, is not constant as it is with rotating systems. The specific efficiency, η_s, is calculated per Eq. (9) using the actual swept area of the oscillation based on the average measured stroke within an analysis window. The total efficiency, η_t, is calculated per Eq. (10) using the design swept area, $A_{\text{swept,design}}$, assuming full ±30 deg motion of the suspension arms. The design swept area is 5.20 m^2 for the large bluff body and 3.53 m^2 for the small bluff body.

$$P_{\text{swept}} = \frac{\rho A_{\text{swept}} v^3}{2} \tag{8}$$

$$\eta_s = \frac{P_{\text{elec}}}{P_{\text{swept}}} \tag{9}$$

$$\eta_t = \frac{P_{\text{elec}}}{P_{\text{swept,design}}} \tag{10}$$

As this is a full-scale prototype, all data are presented in the dimensional form. At the end of Sec. 3, summary nondimensional results are presented to facilitate comparison to work at other scales.

3.1 Error and Uncertainty.

The pulsed, rather than continuous, power output of the oscillatory system complicates data processing and analysis. Furthermore, all tests were conducted under uncontrolled and time-varying flow conditions, with no ability to maintain precise conditions from one system configuration to another. Due to the nonlinearity of damping and spring forces, introduced by the geometry of the tether coupling to the oscillator, and hysteresis, introduced by friction throughout the system, inherent in both the spring and PTO systems, the spring connection position setting and load bank resistance setting are used as the independent variables. Thus, analysis here is tailored to provide correlational insights into the effects of relative changes in spring stiffness and damping on the dependent variables of oscillation frequency and amplitude, and on electrical power output and water-to-wire efficiency.

Neither oscillation frequency nor stroke is affected by instrument offset error and thus are plotted with bars showing the standard deviation of calculated values across data for each configuration. Calculated average electrical power propagates instrument uncertainty. Efficiency calculations propagate uncertainty in streamwise velocity measurements and electrical power and are based on the designed swept area without uncertainty. The power-weighted average and standard deviation, where appropriate, for streamwise

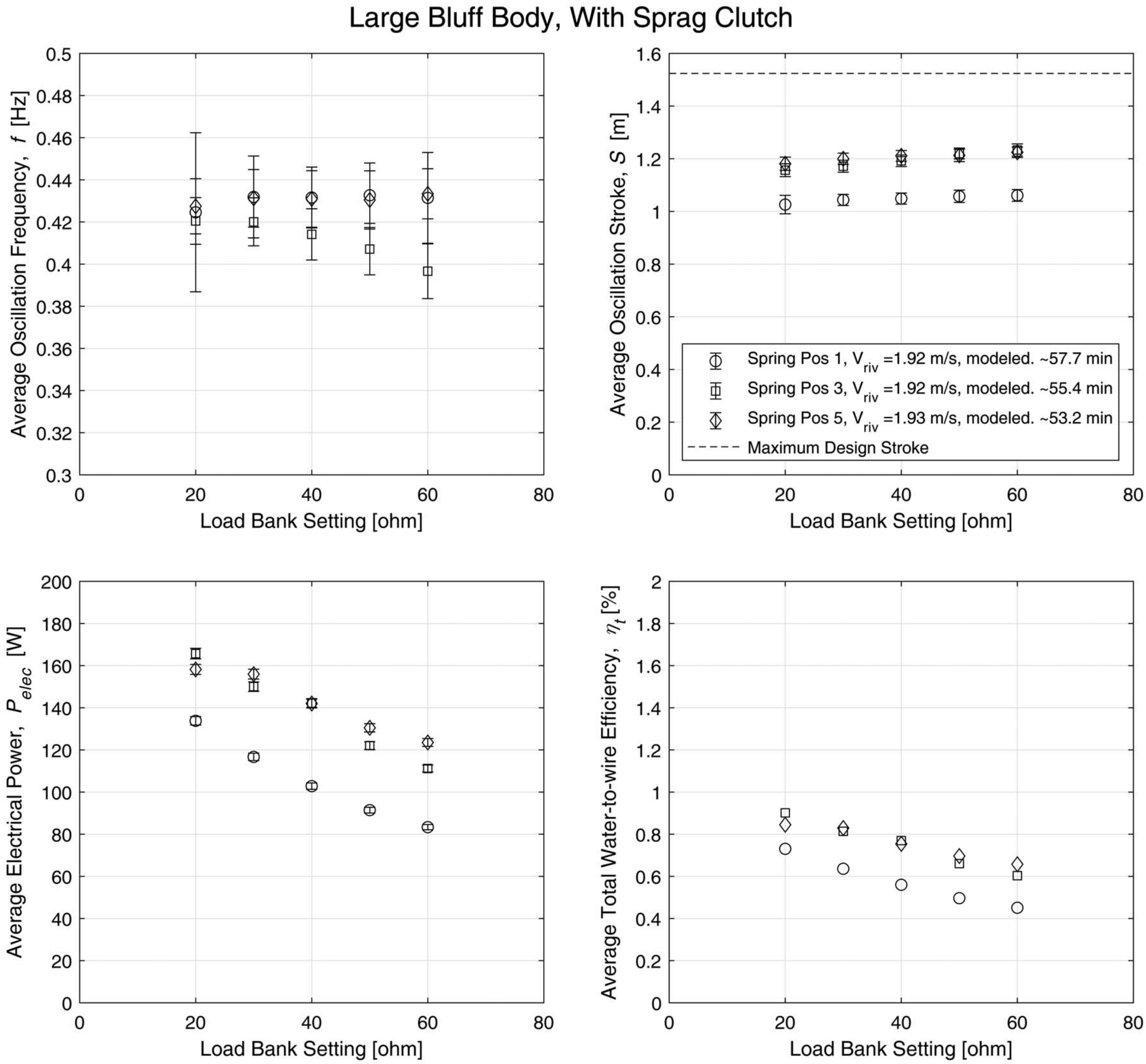

Fig. 11 Correlational plots for large bluff body and sprag clutch configuration. Standard deviations are shown for frequency and stroke. Propagated measurement uncertainty is shown for calculated electrical power. Uncertainty omitted for total efficiency due to use of modeled velocity.

velocity during each deployment interval are noted in the legends in Figs. 11–14. While streamwise velocity cannot be controlled in field testing, the reported mean velocities for tests within each set of plots are within 1% and deemed appropriate for comparison of data in absolute terms. Nondimensional analysis is provided at the end of Sec. 3 to facilitate comparison to other works in the literature.

3.2 Large Bluff Body Performance Correlations.

With the spring tether connected to the spring lever at position 1 (stiffest setting), the system was deployed into the river for a total of 58 min, with approximately 10 min of operation at each of five load bank settings, as shown in Table 4. The system was then removed from the water, the tether connection was changed, and then the system was re-deployed and again stepped through a range of load bank settings. The data were binned for each load bank setting and are plotted in Fig. 11 with bars for standard deviation or uncertainty as described earlier. During these tests, neither the ADCP nor ADV data are available; however, USGS stream discharge data have been correlated to ADCP measurements to provide modeled velocity, with no reported standard deviation or uncertainty. Note that load bank settings below 20 ohms resulted in significant belt slippage in the PTO and were not explored further. In general, softer spring settings (higher digit spring position) resulted in a larger stroke of oscillation.

3.3 Small Bluff Body Performance Correlations.

The same methodology was used for a similar set of deployments with the small bluff body installed. During these tests, ADCP data are available and are presented with the associated uncertainty (Fig. 12).

3.4 Comparison of Small and Large Bluff Body Performance.

To compare the performance of the two bluff body sizes, data for both bluff bodies with spring setting 3 are plotted in Fig. 13. The large bluff body produced larger amplitude oscillations at a lower frequency while producing similar electrical output, resulting in a lower η_t efficiency based on the maximum design swept area, $A_{\mathrm{swept,design}}$, for each oscillator.

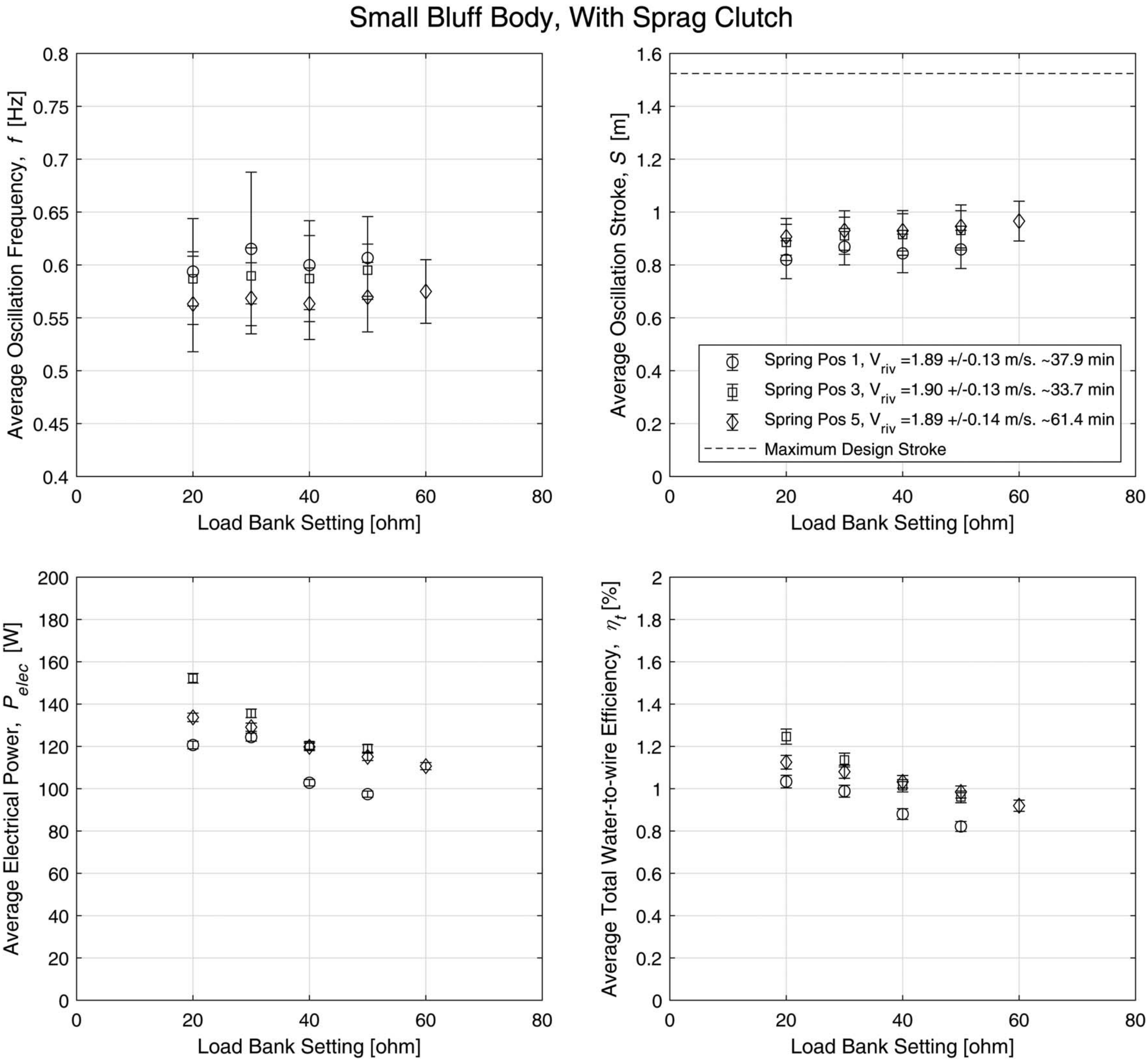

Fig. 12 Performance correlations for Water Horse prototype with small bluff body and sprag clutch installed. Standard deviations are shown for frequency and stroke. Propagated measurement uncertainty is shown for calculated electrical power and water-to-wire efficiency.

3.5 Mechanical Rectification Performance Assessment. On the final day of testing, the mechanical rectifier (sprag clutch) was removed, and the system was allowed to rotate the PMG bidirectionally. As shown in Fig. 14, this resulted in similar oscillation amplitude and frequency with a significant increase in power output and efficiency. It should be noted that average velocity was approximately 6% higher (19% greater hydrokinetic power) during testing without mechanical rectification.

3.6 Nondimensional Analysis

3.6.1 Specific Efficiency Versus Reynolds. For consistency, all results mentioned earlier used the maximum design swept area as the basis for efficiency calculations. Figure 15 presents the specific efficiency, η_s, for each testing configuration, which reflects the efficiency based on the swept area as measured by the amplitude of the oscillations. The configurations are a large bluff body with mechanical rectification (as described in Sec. 2.2.3), a small bluff body with mechanical rectification, and small bluff body without mechanical rectification (“w/o Sprag”). Data are presented on the basis of Reynolds number to account for differences in bluff body size and flow velocity. One possible explanation for the lower efficiency of the large bluff body is that significant energy generated by the bluff body was observed to transfer into the barge. One possible explanation for the higher efficiency of the small bluff body without the sprag clutch is that the generator was coupled to the oscillator for both the outward and inward portions of bluff body oscillations, reducing the peak-to-average power output. Both of these possibilities are explored further in Sec. 4. Table 5 summarizes the highest efficiency data point for each of the three configurations.

3.6.2 Amplitude Versus Reynolds. To provide a comparison to other published FIO results, the data presented earlier are plotted with nondimensional amplitude, $A^* = A/D$ versus Reynolds number in Fig. 16. Due to the asymmetry of oscillations, the amplitude, A, is taken as half of the full oscillation stroke, S.

3.6.3 Strouhal Versus Reynolds. The Water Horse prototype exhibited evidence of hard galloping, as it was possible to deploy the system slowly and not observe oscillations to initiate until a displacement was externally imposed on the oscillator. This supports the hypothesis that the FIO is driven by lift generated by the relative

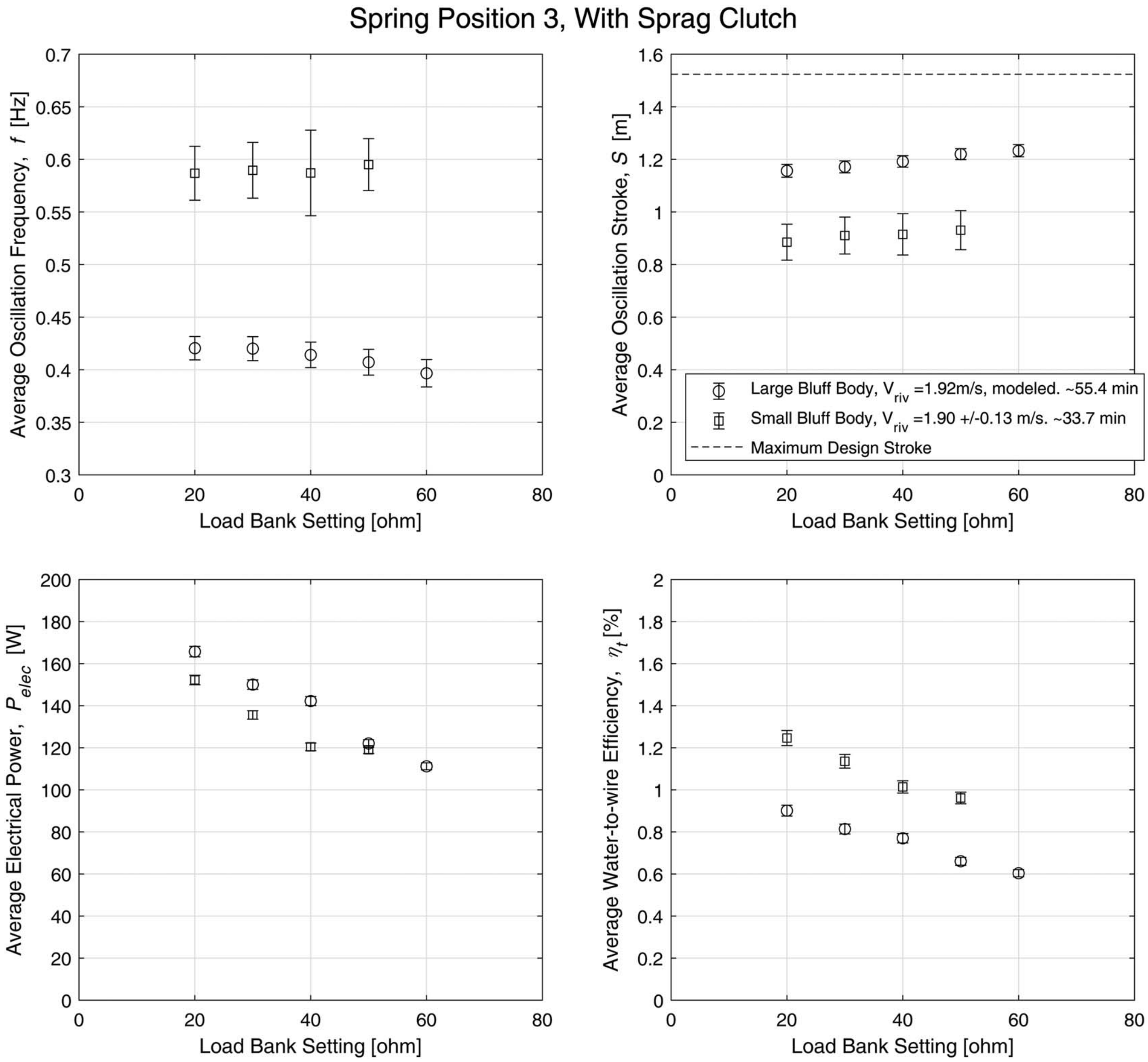

Fig. 13 Performance comparison of Water Horse prototype with small and large bluff bodies. Both with spring position 3 and sprag clutch installed. Standard deviations are shown for frequency and stroke. Propagated measurement uncertainty is shown for calculated electrical power and water-to-wire efficiency.

angle of attack of the flow over the D-shaped bluff body rather than vortex shedding. For completeness, the Strouhal number is presented as a function of the Reynolds number, including standard deviation within each testing window. The Strouhal number is calculated per Eq. (11).

$$\mathrm{St} = \frac{f D_{\mathrm{bluff}}}{v} \tag{11}$$

Here, the characteristic length is taken as the bluff body diameter, and the frequency is the average oscillation frequency observed during the testing window. The results are plotted in Fig. 17 and are lower that the Strouhal value of approximately 0.16 for Reynolds in the range of 2000–20,000 reported in the literature for D-shaped bluff bodies oriented into the flow [20].

4 Discussion

Field testing results are inherently impacted by the lack of control over flow conditions. Furthermore, nonlinearities inherent to the design and unknown nonconservative forces prevent the accurate assessment of average or instantaneous spring and damping coefficients. The net force on the bluff body cannot be resolved from the spring and PTO measurements due to the unknown frictional losses in the suspension pivots, idler pulleys, or spring lever pivots, among other sources of friction and loss. For these reasons, this analysis is limited to correlational analysis of system-level performance parameters based on system configurations and settings.

While IEC 62600-300 prescribes a power performance assessment methodology, it was developed for evaluating the performance of commercially ready systems, which include power converters and controls, during long-duration deployments. In a research and development setting, where the focus is on understanding the impact of system parameters on performance, the IEC standards are not well suited for research and development applications. For this reason, the IEC standard is used to inform instrumentation and data analysis methodologies but is not followed explicitly. Given the nascent nature of riverine hydrokinetic technologies, IEC could consider prescribing methodologies for research and development-focused data analysis. In this analysis, 10 min averages at each system configuration

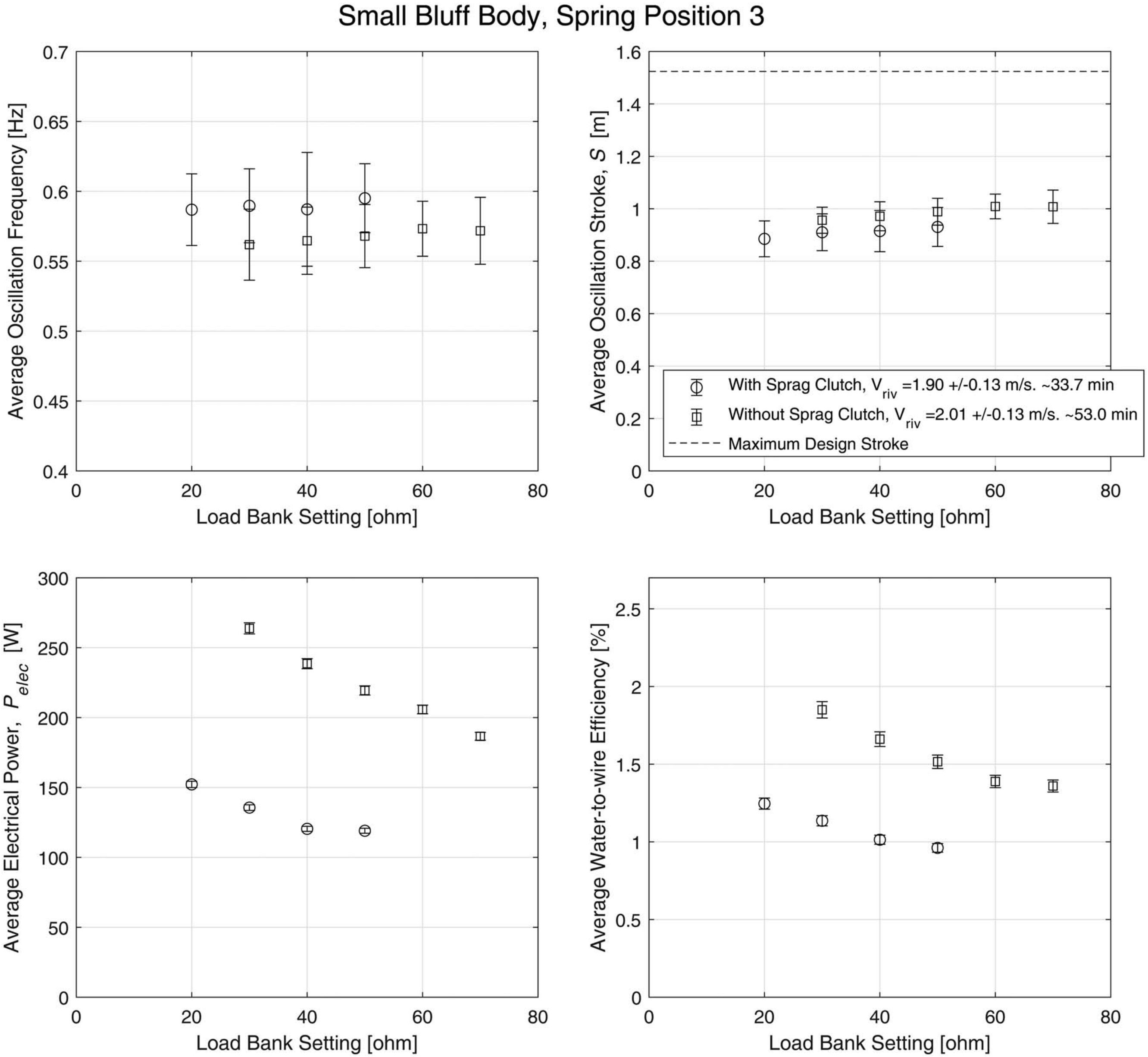

Fig. 14 Performance comparison of Water Horse prototype with and without mechanical rectification. Standard deviations are shown for frequency and stroke. Propagated measurement uncertainty is shown for calculated electrical power and water-to-wire efficiency.

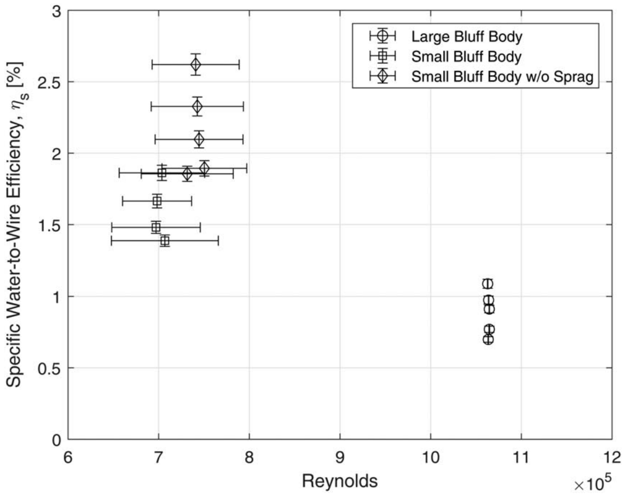

Fig. 15 Specific efficiency versus Reynolds number for three primary configurations across range of reported load bank settings. Reynolds numbers for large bluff body conditions are presented without standard deviation as it uses a modeled velocity estimate.

are used to assess the performance of the system under those settings.

4.1 Correlations Summary. Across all testing configurations, oscillation frequency was observed to vary significantly between the two bluff body diameters tested. Frequency trends with respect to damping and spring stiffness are within the uncertainty of the data and are not evaluated. Relative spring stiffness was highest for spring position 1 and lowest for spring position 5. Oscillation amplitude was generally higher for lower spring and lower damping (higher load bank resistance), as would be expected. Electrical power rose with increased damping; however, belt slippage limitations of the PTO prevented reaching peak power output for any configuration. The specific efficiency, which accounts for the actual swept area, is more representative of the potential efficiency for an optimized system that utilizes its full design stroke.

4.2 Rectification Findings. The relative performance of the system with and without mechanical rectification via sprag clutch was distinctly different. Without any additional rotational inertia, the generator slowed to a stop within each oscillation for all damping values. While adding a flywheel would theoretically enable the generator to provide more steady voltage output, the duration of engagement of the sprag clutch would be reduced, and the inertia coupled to the oscillator during engagement would be increased. Removing the sprag clutch and allowing the PMG to rotate bidirectionally doubled the number of electrical power pulses within each oscillation by coupling the generator to the PTO during the return motions of the oscillator. Evaluation of time-series data, a subset of which is shown in Fig. 18, demonstrates a reduction in peak-to-average electrical power from 7.8 to 4.7 with the removal of mechanical rectification.

Peak-to-average power output has significant impacts on system costs. Generator cost is proportional to generator power rating, and the generator rating must be sufficient to accommodate the peak power levels of the PTO. However, the value of the energy produced by the system is proportional to the average power output. Thus, low peak-to-average ratios indicate higher utilization of the generator with positive implications for LCOE.

4.3 Floating Platform Observations. During operation, significant motion transfer into the floating barge was observed, indicating a reduction in relative motion between the bluff body and the PTO and an associated transfer of force from the bluff body into the barge rather than into the PTO system. Barge heave was notably more severe during large bluff body operation than small bluff body operation. A cursory investigation of accelerometer data shows the difference in magnitude and phase shift between the two test conditions. While data collected on barge heave are not sufficiently rigorous for detailed analysis, these data show the importance of deliberate floating platform design for vertically oscillating hydrokinetic systems. In Fig. 19, the vertical acceleration of the oscillator and barge are overlayed for representative data for the small and large bluff bodies. In the small bluff body data, the zero crossings between the two signals are less synchronized than for the large bluff body data. Furthermore, the peak barge accelerations are lower for the small than the large bluff body.

4.4 Debris Interactions. Field testing provided for a qualitative assessment of the system's performance under exposure to woody debris. The system was observed to survive small to medium impacts without damage or entanglement, while two large debris impacts resulted in breakage of the shear bolts in the breakaway mechanism as designed. Repair of the breakaway mechanism was rapid and entailed tipping the system out of the water, allowing the lower bluff body support to hinge back into place, and installing and torquing two replacement shear bolts.

4.5 Design Shortcomings. The field testing campaign revealed several shortcomings of the prototype design. A primary observation is that the design of the PTO coupling via the spring tether chain, while providing minimal damping at the midstroke, decoupled the generator from the oscillator just as the oscillator was at maximum relative velocity and generating maximum lift force. Another observation was that the belt connection between the primary and secondary PTO shafts, while providing a valuable increase in shaft speed, was observed to slip under low resistance settings, and precluded operation at high damping. Finally, the chain tether for the spring system, while rugged, was noisy

Table 5 Values relevant to efficiency and Reynolds calculations for the highest efficiency damping setting tested with each of three configurations of bluff body and mechanical rectification tested

Parameter	Units	Large bluff body	Small bluff body	Small bluff body without sprag clutch
Bluff body diameter, D_{bluff}	m	0.61	0.41	0.41
Average streamwise velocity, v	m/s	1.92	1.91	2.01
Average swept area, A_{swept}	m^2	4.31	2.36	2.49
Average swept kinetic power, P_{swept}	W	15,200	8,170	10,100
Average electrical output power, P_{elec}	W	165	152	264
Reynolds number, Re	n/a	1,063,000	703,600	740,800
Specific efficiency, η_s	%	1.09	1.86	2.62

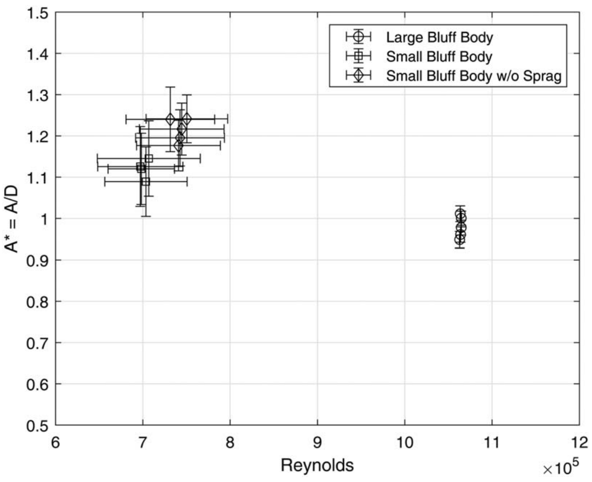

Fig. 16 A/D versus Reynolds number, with standard deviations, for primary configurations of interest across reported load bank settings. Reynolds numbers for large bluff body conditions are presented without standard deviation as it uses a modeled velocity estimate.

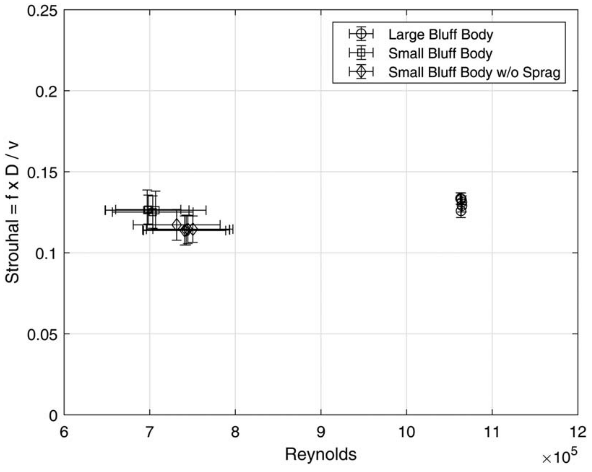

Fig. 17 Strouhal number versus Reynolds number, with standard deviations, for configurations of interest. Reynolds numbers for large bluff body conditions are presented without standard deviation as it uses a modeled velocity estimate.

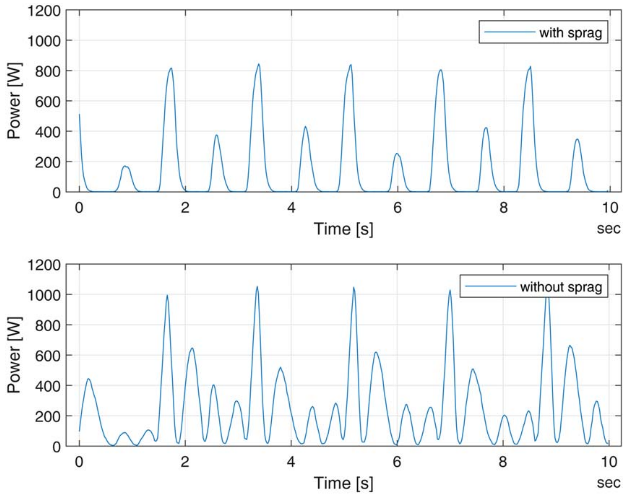

Fig. 18 Electrical power signal for small bluff body with (top) and without (bottom) mechanical rectification presented to show qualitative effect of removing the sprag clutch. The flow speed averaged 1.88 m/s in the upper plot and 1.98 m/s in the lower plot.

(inefficient) and would be a high maintenance item due to exposed lubricated surfaces.

The design process revealed the challenge of designing a simultaneously high-stiffness and high-displacement spring system, and the prototype spring system showed significant wear at the friction surfaces that were under high force, up to 35 kN (8000 lbf) at the spring pack pushrod. Again, this is a source of energy loss and increased maintenance requirements.

Investigations into the accelerometer data did not show significant off-axis loading or vibration, reducing the associated design requirements for suspension arms in future prototypes. Similarly, strain gauge measurements on the lower suspension arm showed large margins of safety, indicating a potential for reduced material cost in future suspension designs.

Finally, future prototypes should attempt to minimize the motion transfer into the barge by operating at higher oscillation frequency and with more uniform PTO engagement to reduce energy loss into barge heave. An ongoing challenge for all FIO systems will be the pulsed power signal and improving peak-to-average utilization of

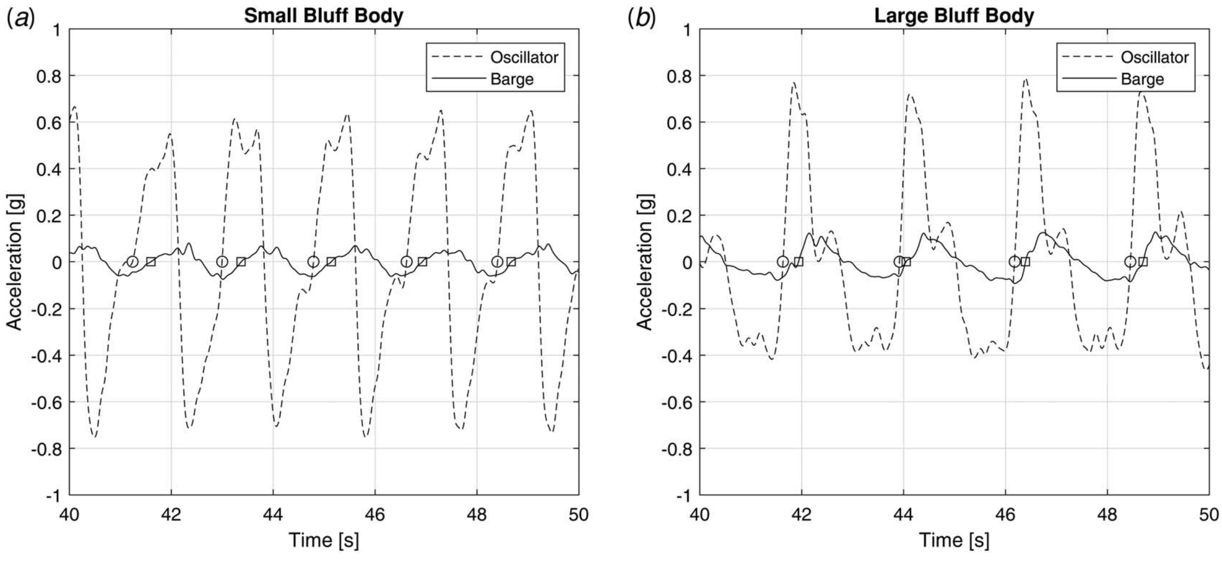

Fig. 19 Small bluff body acceleration signals (left) and large bluff body acceleration signals (right). Filtered zero crossings notated to show phase shift.

generator components to increase capacity factor and decrease LCOE.

5 Conclusions and Future Work

A future publication will disseminate the design improvements of a second Water Horse prototype informed by the testing described in this paper. This second prototype incorporates design changes to the bluff body, suspension, PTO, and spring systems. Bluff body diameter is reduced to increase oscillation frequency, the suspension is redesigned for simplicity and to reduce frictional losses, the PTO is redesigned to maximize coupling to the oscillator at midstroke, and the spring system is reconfigured to reduce friction and improve packaging. In addition, push-testing is completed to explore the power curve of the system across a broader range of inflow velocities. The future prototype also incorporates two oscillators, arranged upstream–downstream to investigate the impact of flow disruptions on downstream systems.

Acknowledgment

The authors would like to acknowledge the Nenana Native Council for their long-running support of the Tanana River Test Site and land use agreements that permit our use of the river bank. We acknowledge TRTS manager Stephanie Fisher and graduate student Emily Browning for their critical contributions supporting field testing activities. We acknowledge Andy Seitz, Mark Evans, and Taylor Poirrier of the UAF College of Fisheries and Ocean Sciences for performing fish sampling and reporting during field testing. We acknowledge Jon Holmgren and Tim Manning for their expert fabrication and assembly of this most unusual contraption. We acknowledge Lisa Weiland and Scott Kennedy of Renerge, Inc. for their prior development of Water Horse intellectual property and for their technical input and review on the development of this work.

Funding Data

- The U.S. Department of Energy's Office of Energy Efficiency and Renewable Energy (EERE) under the Water Power Technologies Office (WPTO) Award Number DE-EE0008389.

Conflict of Interest

There are no conflicts of interest.

Data Availability Statement

The data and information that support the findings of this article are freely available [42].

Nomenclature

c = damping coefficient (N-m-s/rad)
k = spring stiffness
v = streamwise water velocity
A = amplitude defined as half-stroke, $S/2$
D = bluff body diameter
L = bluff body length
S = stroke, $Z_{\text{osc, max}} - Z_{\text{osc, min}}$
d_1 = primary PTO pulley diameter
d_2 = secondary PTO pulley diameter
d_{idler} = tether idler pulley diameter
f_n = oscillation frequency of cycle, n (Hz)
k_{spring} = individual spring constant
l_{arm} = linkage length
l_{offset} = idler offset from oscillator
l_{pivot} = spring lever length
l_{tether} = tether lever length
m_{osc} = oscillating mass
r_{belt} = PTO belt speed ratio, d_1/d_2
t_n = start time of cycle, n (s)
A_{swept} = actual swept area of oscillation stroke
$A_{\text{swept,design}}$ = design swept area at full stroke
I_{DC} = DC current N_{kp} = number of springs in parallel
N_{ks} = number of spring levels in series
N_{sprocket} = PTO sprocket tooth count
P_{elec} = electric output power
P_{swept} = kinetic power of swept area
p_{tether} = tether chain pitch (cm/tooth)
V_{DC} = DC output voltage
Z_{osc} = vertical position of oscillator from midstroke
$A*$ = nondimensional amplitude, A/D
rpm = shaft revolutions per minute
ACEP = Alaska Center for Energy and Power
ADCP = acoustic Doppler current profiler
ADV = acoustic Doppler velocimeter
CEC = current energy converter
COTS = commercial off-the-shelf
DC = direct current
FIO = flow-induced oscillation
IEC = International Electrotechnical Commission
LCOE = levelized cost of energy
MR = mass ratio (oscillating mass divided by displaced water mass at midstroke)
O&M = operations and maintenance
PMG = permanent magnet generator
PTO = power takeoff
Re = Reynolds number
St = Strouhal number
TRTS = Tanana River Test Site
UAF = University of Alaska Fairbanks
USGS = United States Geological Survey
η_s = specific conversion efficiency (actual swept area)
η_t = total conversion efficiency (design swept area)
θ = angular position of suspension
θ_{max} = max linkage angle
ρ = density of water
ω = angular velocity of suspension (rad/s)

References

[1] Alaska Energy Authority, 2002, "FY22 PCE Community Report.Pdf," https://www.akenergyauthority.org/Portals/0/Power Cost Equalization/FY22 PCE Community Report.pdf, Accessed December 20, 2024.

[2] Meacham, C. P., and Clark, J. H., 1994, *Pacific Salmon Management – The View from Alaska*, Alaska Fishery Research Bulletin, Vol. 1, No. 1, pp. 76–80.

[3] Courtney, M. B., Flanigan, A. J., Hostetter, M., and Seitz, A. C., 2022, "Characterizing Sockeye Salmon Smolt Interactions With a Hydrokinetic Turbine in the Kvichak River, Alaska," N. Am. J. Fish. Manage., **42**(4), pp. 1054–1065.

[4] Seitz, A. C., Moerlein, K., Evans, M. D., and Rosenberger, A. E., 2011, "Ecology of Fishes in a High-Latitude, Turbid River With Implications for the Impacts of Hydrokinetic Devices," Rev. Fish Biol. Fish., **21**(3), pp. 481–496.

[5] Bradley, P. T., Evans, M. D., and Seitz, A. C., 2015, "Characterizing the Juvenile Fish Community in Turbid Alaskan Rivers to Assess Potential Interactions With Hydrokinetic Devices," Trans. Am. Fish. Soc., **144**(5), pp. 1058–1069.

[6] Copping, A. E., and Hemery, L. G., 2020, "OES-Environmental 2020 State of the Science Report: Environmental Effects of Marine Renewable Energy Development Around the World," Report for Ocean Energy Systems (OES), PNNL–29976, 1632878.

[7] Ravens, T., 2014, *Alaska In-River Hydrokinetic Energy Resources*, University of Alaska Anchorage, Alaska Energy Authority.

[8] Brown, E. J., King, A. L., Duvoy, P. X., Trochim, E., Kasper, J. L., Wilson, M. L., and Ravens, T. M., 2023, "Site Suitability Analysis of Hydrokinetic River Energy Resources at Community Microgrids on the Kuskokwim River, Alaska," Renewable Energy, **217**, p. 119083.

[9] Johnson, J., and Pride, D., 2010, *River, Tidal, and Ocean Current Hydrokinetic Energy Technologies: Status and Future Opportunities in Alaska*, Alaska Center for Energy and Power, Fairbanks, AK.

[10] Worthington, M., Ali, M., and Ravens, T., 2013, "Abrasion Testing of Critical Components of Hydrokinetic Devices," Final Scientific Report, 1110808.

[11] Salmon, A., Meadows, B., Kilcher, L., and Hirsh, B., 2022, *Igiugig's Journey Toward Sustainability*, National Renewable Energy Laboratory.

[12] Toniolo, H., Duvoy, P., Vanlesberg, S., and Johnson, J., 2010, "Modelling and Field Measurements in Support of the Hydrokinetic Resource Assessment for the Tanana River at Nenana, Alaska," Proc. Inst. Mech. Eng. Part A J. Power Energy, **224**(8), pp. 1127–1139.

[13] Johnson, J. B., Kasper, J. L., Schmid, J., Duvoy, P., Kulchitsky, A., Mueller-Stoffels, M., Konefal, N., and Seitz, A. C., 2015, *Surface Debris Characterization and Mitigation Strategies and Their Impact on the Operation of River Energy Conversion Devices on the Tanana River at Nenana, Alaska*, Alaska Center for Energy and Power, Fairbanks, AK.

[14] Browning, E., Olson, S., Fao, R., Keester, A., and McVey, J., 2023, "Tanana River Test Site Model Verification Using the Marine and Hydrokinetic Toolkit (MHKiT)," Energies, **16**(8), p. 3326.

[15] Johnson, J., Schmid, J., Kasper, J., Seitz, A., and Duvoy, P., 2014, "Protection of In-River Hydrokinetic Power-Generating Devices From Surface Debris in Alaskan Rivers," University of Alaska, Fairbanks, AK, https://tethys-engineering.pnnl.gov/publications/protection-river-hydrokinetic-power-generating-devices-surface-debris-alaskan-rivers, Accessed August 22, 2022.

[16] Jump, S., Courtney, M. B., and Seitz, A. C., 2019, "Vertical Distribution of Juvenile Salmon in a Large Turbid River," J. Fish Wildl. Manage., **10**(2), pp. 575–581.

[17] Kasper, J. L., Johnson, J. B., Duvoy, P. X., Konefal, N., and Schmid, J., 2015, *A Review of Debris Detection Methods*, Northwest National Marine Renewable Energy Center, Fairbanks, AK.

[18] Novak, M., 1972, "Galloping Oscillations of Prismatic Structures," J. Eng. Mech. Div., **98**(1), pp. 27–46.

[19] Parkinson, G. V., and Brooks, N. P. H., 1961, "On the Aeroelastic Instability of Bluff Cylinders," ASME J. Appl. Mech., **28**(2), pp. 252–258.

[20] Blevins, R. D., 1977, *Flow-induced vibration*, Van Nostrand Reinhold Company, New York.

[21] Billah, K. Y., and Scanlan, R. H., 1991, "Resonance, Tacoma Narrows Bridge Failure, and Undergraduate Physics Textbooks," Am. J. Phys., **59**(2), pp. 118–124.

[22] Lv, Y., Sun, L., Bernitsas, M. M., and Sun, H., 2021, "A Comprehensive Review of Nonlinear Oscillators in Hydrokinetic Energy Harnessing Using Flow-Induced Vibrations," Renewable Sustainable Energy Rev., **150**, p. 111388.

[23] Bernitsas, M. M., 2011, "The VIVACE Converter, Enhancing Flow Induced Motions to Harness Hydrokinetic Energy in an Environmentally Compatible Way," Marine and Hydrokinetic Device Modeling Workshop, National Wind Technology Center, Boulder, CO.

[24] Bernitsas, M. M., Raghavan, K., Ben-Simon, Y., and Garcia, E. M. H., 2008, "VIVACE (Vortex Induced Vibration Aquatic Clean Energy): A New Concept in Generation of Clean and Renewable Energy From Fluid Flow," ASME J. Offshore Mech. Arct. Eng., **130**(4), p. 041101.

[25] Chang, C. C., Ajith Kumar, R., and Bernitsas, M. M., 2011, "VIV and Galloping of Single Circular Cylinder With Surface Roughness at $3.0 \times 104 \leq \mathrm{Re} \leq 1.2 \times 105$," Ocean Eng., **38**(16), pp. 1713–1732.

[26] Ding, W., Sun, H., Xu, W., and Bernitsas, M. M., 2019, "Numerical Investigation on Interactive FIO of Two-Tandem Cylinders for Hydrokinetic Energy Harnessing," Ocean Eng., **187**, p. 106215.

[27] Kim, E. S., Bernitsas, M. M., and Ajith Kumar, R., 2013, "Multicylinder Flow-Induced Motions: Enhancement by Passive Turbulence Control at $28{,}000 < \mathrm{Re} < 120{,}000$," ASME J. Offshore Mech. Arct. Eng., **135**(2), p. 021802.

[28] Ma, C., Sun, H., Nowakowski, G., Mauer, E., and Bernitsas, M. M., 2016, "Nonlinear Piecewise Restoring Force in Hydrokinetic Power Conversion Using Flow Induced Motions of Single Cylinder," Ocean Eng., **128**, pp. 1–12.

[29] Modir, A., and Goudarzi, N., 2019, "Experimental Investigation of Reynolds Number and Spring Stiffness Effects on Vortex Induced Vibrations of a Rigid Circular Cylinder," Eur. J. Mech. B Fluids, **74**, pp. 34–40.

[30] Raghavan, K., and Bernitsas, M. M., 2011, "Experimental Investigation of Reynolds Number Effect on Vortex Induced Vibration of Rigid Circular Cylinder on Elastic Supports," Ocean Eng., **38**(5–6), pp. 719–731.

[31] Sun, H., Kim, E. S., Nowakowski, G., Mauer, E., and Bernitsas, M. M., 2016, "Effect of Mass-Ratio, Damping, and Stiffness on Optimal Hydrokinetic Energy Conversion of a Single, Rough Cylinder in Flow Induced Motions," Renewable Energy, **99**, pp. 936–959.

[32] Kim, E. S., and Bernitsas, M. M., 2016, "Performance Prediction of Horizontal Hydrokinetic Energy Converter Using Multiple-Cylinder Synergy in Flow Induced Motion," Appl. Energy, **170**, pp. 92–100.

[33] Weiland, L., and Kennedy, S., 2019, "Fluid Flow Induced Oscillating Energy Harvester With Variable Damping Based Upon Oscillation Amplitude," US Patent US10378507B2.

[34] Weiland, L., and Kennedy, S., 2019, Fluid Flow Induced Oscillating Energy Harvester Maximizing Power Output through Off-Center Mounted Toggling Bluff Body and/or Suspension Stiffening Mechanism," US Patent US20170234294A1.

[35] Kristufek, M., 2013, "On the Use of Computational Fluid Dynamics for Evaluation of Nonlinear Hydrodynamic Galloping Energy Harvester Performance," Master's Thesis, University of Pittsburgh (unpublished).

[36] Wise, M., and Al-Badri, M., 2021, "Energy Conversion Unit for Low-Speed Vertical Oscillator Hydrokinetic Energy Harvester," 2021 IEEE International Electric Machines & Drives Conference (IEMDC), Hartford, CT, pp. 1–6.

[37] Wise, M., Al-Badri, M., Loeffler, B., and Kasper, J., 2021, "A Novel Vertically Oscillating Hydrokinetic Energy Harvester," 2021 IEEE Conference on Technologies for Sustainability (SusTech), Orange County, CA, pp. 1–8.

[38] Todd, G. L., 1994, *A Lightweight, Inclined-Plane Trap For Sampling Salmon Smolts in Rivers*, Alaska Fishery Research Bulletin.

[39] USGS, "USGS 15515500 TANANA R AT NENANA AK," https://waterdata.usgs.gov/nwis/inventory/?site_no=15515500, Accessed December 20, 2022.

[40] Walsh, C., Fochesatto, J., and Toniolo, H., 2012, "The Importance of Flow and Turbulence Characteristics for Hydrokinetic Energy Development on the Tanana River at Nenana, Alaska," Proc. Inst. Mech. Eng. Part A J. Power Energy, **226**(2), pp. 283–299.

[41] Manning, R., 1891, "On the Flow of Water in Open Channels and Pipes," Trans. Inst. Civ. Eng. Irel., **20**, p. 161.

[42] Loeffler, B., Duvoy, P., Browning, E., and Kasper, J., 2020, "Water Horse Hydroelectric Harvester Single Oscillator Field Testing Data, UAF—Nenana Alaska, 2020," https://mhkdr.openei.org/submissions/465.